Metals & corrosion

Effects of pre-stretching on corrosion resistance of a creep-aged Al–5.87Zn–2.07Mg–2.42Cu alloy

Hanfang Dai[1], Guofu Xu[1,2], Yao Li[1], and Xiaoyan Peng[1,*]

[1] School of Materials Science and Engineering, Central South University, Hunan 410083, Changsha, China
[2] Key Laboratory of Nonferrous Materials Science and Engineering of Ministry of Education, Hunan 410083, Changsha, China

ABSTRACT

In this experiment, the corrosion resistance of an Al–5.87Zn–2.07 Mg–2.42Cu alloy with different pre-stretchings (0, 2, 4, 6%) after creep aging (CA) was investigated. It is found that the corrosion performance reaches the optimal value at 4% pre-stretched sample, which owns the largest stress corrosion sensitivity factor r_{tf} (93.8%) and the shallowest intergranular corrosion depth (24.7 μm). When the degree of pre-stretching before CA rises, coarser and sparser intragranular precipitates (IGPs) are observed after CA. The average size of IGPs rises from about 2.2 to 5.8 nm while the density declines from about 5.4×10^{16} to 3.5×10^{16} cm^{-3}, and thus diminish the electron scattering effect and release the strain field. Moreover, the grain boundary precipitates (GBPs) become larger and more discontinuous and the precipitate-free zones (PFZs) broaden. The average size of GBPs rises from about 9.3 to 23.9 nm, and the average distance between GBPs increases from about 11.8 to 39.4 nm. Additionally, the segregation degree of Mg reduces and the content of Cu of GBPs rises with the increase of pre-stretching. These influence factors reduce the possibility of anodic dissolution and hydrogen-induced cracking (HIC). However, the expanding PFZ increases the potential difference between matrix and PFZ, promoting the anodic dissolution. Therefore, the corrosion resistance of an Al–5.87Zn–2.07 Mg–2.42Cu alloy can be improved by applying 4% pre-stretching before CA.

Introduction

Al–Zn–Mg–Cu alloys are used in aerospace industry extensively due to its high strength, low density and excellent fabricability [1, 2]. With the rapid development of high-end equipment, the overall panels tend to be large in volume, complex in structure, uneven in thickness and variable in curvature. Thus, higher requirements are put forward for dimensional accuracy and material performance after forming [3, 4]. Therefore, it is urgent to develop advanced, accurate and efficient aerospace components by using Al–Zn–Mg–Cu alloys. Creep age forming is a way to synchronize the forming and the heat treatment of the workpiece under a demanded temperature and stress, greatly improving the forming efficiency [5]. Under the integral demands of precise forming and performance enhancement, creep aging (CA) system plays a key role in the deformation mechanism and further affecting the formability of the workpiece. Moreover, the service environment of modern aerospace equipment has been extreme and the aerospace equipment is inevitable to contact with various corrosive media [6]. Therefore, it is of great significance to explore methods to improve the corrosion resistance of Al–Zn–Mg–Cu alloy based on CA behavior.

In order to understand the CA behavior of aluminum alloys, many researches have been carried out to explore the microstructure evolution and property improvement of CA process. Jeshvaghani et al. [7, 8] studied an appropriate forming condition (150 °C and 24 h) for 7075 alloy to diminish corrosion susceptibility without weakening mechanical properties after CA. The results show that with the increasing of time and temperature, the number of precipitates and the width of the precipitate-free zones (PFZs) changed. Lei et al. [6] explored the creep aging formability of 7050 aluminum alloy at 165 °C for 18 h relying on the different initial temper (solution, retrogression and re-solution). It concludes that since different obstructions of the precipitates on the movement of dislocations, the alloy with retrogression initial temper has the largest creep strain and the best CA formability. Li et al. [9] combined pre-deformation (0%, 1.5%, 3.0%, and 4.5%) with creep aging to investigate the dynamic interaction between the dislocations and precipitations of 7050 alloy. The precipitations result in a decrease in the mobile dislocation density and creep rate in the first stage of CA and the dislocation multiplication and annihilation reach a dynamic balance, leading to a relatively stable creep rate in the second stage. Deschamps et al. [10] revealed that the accumulation of vacancy supersaturation increases the diffusion rate of solute atoms, promoting the precipitation process during CA at 160 °C in Al–Zn–Mg–Cu alloy. Fribourg et al. [11] studied the precipitate evolution of AA7449 alloy during CA and discovered that an acceleration coarsening of precipitates was induced by applying plastic deformation. Xiao et al. [12] reported that the growth and discontinuous distribution of grain boundary precipitations (GBPs) improve the corrosion resistance of an Al–Zn–Mg–Cu alloy without reducing strength and ductility. Lin et al. [13] found that the temperature affects the size and distribution of precipitates of Al–Zn–Mg–Cu alloy during creep aging, which affects the corrosion resistance significantly. Chen et al. [14] concluded that discontinuous GBPs weaken the degree of intergranular corrosion and the GBPs with higher copper cause lower stress corrosion susceptibility. Based on the above, most investigations are conducted to explore the CA behavior and the effect of microstructure on corrosion performance, but few studied on the influence mechanism of pre-deformation on the corrosion properties of the creep-aged Al–Zn–Mg–Cu alloy.

Therefore, this study focuses on the effect of pre-stretching on microstructure and corrosion resistance of the creep-aged Al–5.87Zn–2.07 Mg–2.42Cu alloy. The slow strain rate testing (SSRT) results, intergranular corrosion properties and microstructure characteristic of creep-aged alloys with different pre-stretchings are compared. The influence of the pre-stretching on the precipitation behavior during CA and the effect of the evolution of the precipitates and content of alloy elements on the corrosion behavior of the creep-aged alloy are discussed.

Experimental procedures

Material preparation and creep aging tests

The as-received material used in this experiment is a kind of semi-continuous casting Al–5.87Zn–2.07 Mg–2.42Cu alloy. The ingot was homogenized at 470 °C for 24 h, cooled to room temperature in air, then kept at 420 °C for 4 h, subsequently hot rolled from 50 to 6 mm in multiple passes, annealing at 350 °C for 1 h and cold

rolled at room temperature to 2.5 mm thickness. Next, the specimens were solution treated at 475 °C for 1 h, rapidly quenched in cold water and the transfer time is less than 5 s. The specimens for CA were wire cut out to a uniform standard. Before conducting the CA tests, the specimens were pre-stretched to 0%, 2%, 4%, 6%, respectively. The pre-stretching treatments were performed on MTS 858 electro-hydraulic servo testing machine with a tensile rate of 2 mm/min. The creep aging experiments were carried out on a R-RC-50 electronic high-temperature creep testing machine. The whole process is depicted in Fig. 1. The creep aging temperature, the testing time and stress were chosen as 140 °C, 20 h and 250 MPa, respectively. After the creep aging, the specimens were cooled in air.

Corrosion properties and microstructure characterization

The stress corrosion cracking (SCC) resistances were assessed by SSRT in air and 3.5 wt.% NaCl solution. The SSRT specimens are performed by RGM-6050 slow stress corrosion equipment with a tensile rate of 9×10^{-4} mm/min. For intergranular corrosion, the samples were immersed in a corrosion solution of 57 g/L NaCl + 10 ml/L H_2O_2 at 35 °C for 6 h. The corroded specimen was cut off 5 mm along the vertical direction of the main deformation and the maximum depth was observed under a Leica metallographic microscope.

To determine the dislocation density variation, X-ray diffraction (XRD) tests were performed on the Rigaku Smartlab X-ray diffractometer operating at
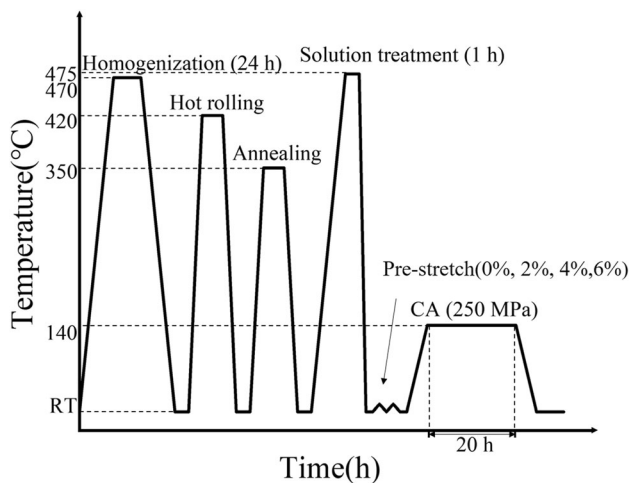

Figure 1 Flow chart for processing the experimental alloy.

40 kV and 30 mA with a scanning speed of 10°/min. The transmission electron microscope (TEM) investigation was conducted by FEI Tecnai G2 F20 transmission electron microscope at 200 kV. Line scanning is performed at scanning transmission electron microscopy (STEM) mode, with the electron beam of 1 nm scanning step. The samples for TEM observations were wire cut, milled to about 80 μm and polished. The 3 mm diameter foils were punched from the slice and then electrolytic double sprayed using an MTP-1 twin-jet polishing system with a mixture of 70% methanol and 30% nitric acid between -30 °C and -20 °C.

Results

Corrosion resistances

Figure 2 shows stress-displacement curves, failure time t_f, stress corrosion sensitivity factor r_{tf} of the creep-aged specimens with various pre-stretchings. As can be seen from Fig. 2a, the stress rises rapidly firstly with the increase of displacement, then slowly rises to the maximum stress, and then the stress begins to decrease until the fracture. The displacement and fracture strength of the specimen applied the same pre-stretching in air are greater than those in corrosive environment. The post-fracture displacement increases and t_f prolongs as the degree of pre-stretching rises. The displacement of the samples in air with 0%, 2%, 4%, 6% pre-stretching is 2.86 mm, 2.79 mm, 3.38 mm, 3.50 mm, respectively, while in 3.5% NaCl solution is 2.31 mm, 2.54 mm, 3.17 mm, 3.25 mm, respectively. The specimen with 4% pre-stretching owns larger post-fracture displacement and longer t_f than the 0% and 2% pre-stretched samples, both in air and corrosive environment. The 6% pre-stretched specimen has the longest displacement before fracture in the air and the stress reaches a peak value, which is lower than other specimens. The stress corrosion sensitivity factor r_{tf} is the main parameter to evaluate the stress corrosion resistance, which can be determined by [15]:

$$r_{tf} = \frac{t_{fe}}{t_{fc}} \tag{1}$$

where t_{fe} is the failure time of the sample in a corrosive environment (3.5 wt.% NaCl solution in this experiment) and t_{fc} is the matching value in the air. The closer r_{tf} is to 1, the lower the stress corrosion
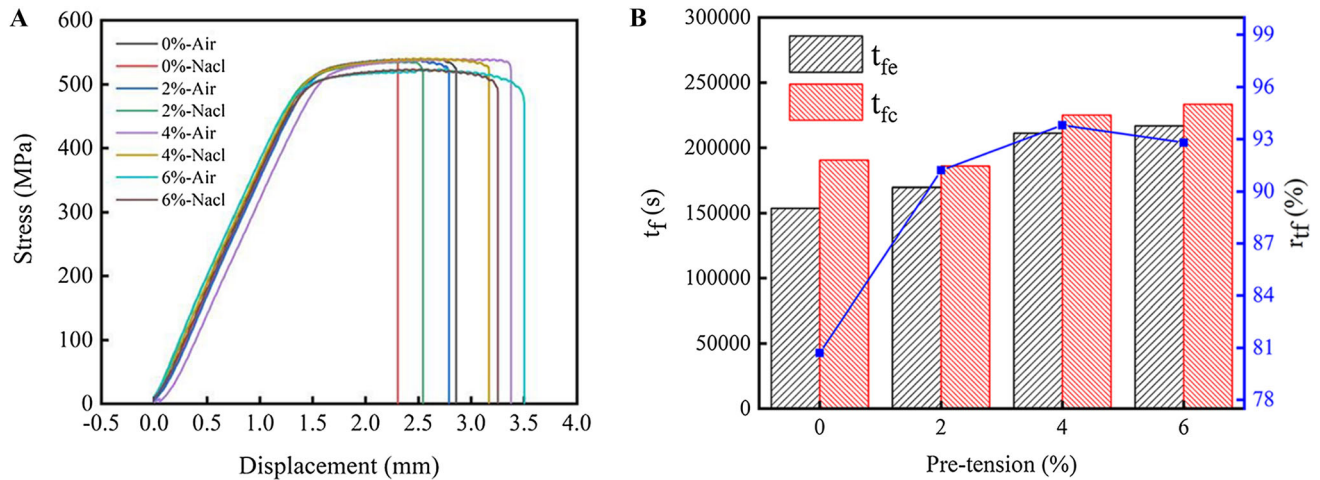
Figure 2 SSRT results of samples with various pre-stretchings after creep aging: **a** stress-displacement curves; **b** failure time t_f, stress corrosion sensitivity factor r_{tf}.

sensitivity of the alloy is, the better the stress corrosion resistance is [16]. Figure 2b displays t_f and r_{tf} of different pre-stretched samples. The r_{tf} of the samples with 0, 2%, 4%, 6% pre-stretching is 80.7%, 91.2%, 93.8%, 92.8%, respectively. The 4% pre-stretched specimen shows the largest r_{tf}. Obviously, the sample with 4% pre-stretching has the best corrosion resistance among these samples.

Figure 3 shows the maximum corrosion depth of cross section of specimens with various pre-stretchings soaked in intergranular corrosion solution for 6 h. Clearly, the alloy without pre-stretching is the most sensitive to intergranular corrosion, and the maximum intergranular corrosion depth reaches 46.8 μm. The maximum intergranular corrosion depth of the alloy with 6% pre-stretching is 33.7 μm, which indicates that the intergranular corrosion resistance is better than that of the 2% pre-deformed sample with 41.6 μm corrosion depth, but still deeper than that of 4% pre-deformed specimen, which is the shallowest (24.7 μm). Therefore, the sample with 4% pre-stretching is speculated to possess the best intergranular corrosion resistance.

Microstructure observations

Evolutions of intragranular precipitates after creep aging

Figure 4 shows the TEM images of intragranular precipitates (IGPs) and corresponding selected area electron diffraction (SAED) patterns of the specimens with

different pre-stretchings (0%, 2%, 4%, 6%) after CA at 140 °C for 20 h. The SAED images of samples are captured along the [001] Al matrix zone axis. As shown in Fig. 4a, a large number of precipitates distribute in the matrix evenly and densely. The diffraction spots appear at 1/3 and 2/3 $\{220\}_{Al}$, indicating that the primary precipitations are η′ phases (Fig. 4b). When the pre-deformations increase to 2%, the change of diffraction spot types is not obvious (Fig. 4c, d). As depicted in Fig. 4e, g, the diameter of precipitates increases and the density drops. The spots at 2/3 $\{220\}_{Al}$ are detected in Fig. 4f, h, which means the presence of η phase. Especially in the 6% pre-stretched specimen, the spots of η are obvious, which means that more η show up in the matrix.

In order to analyze the influence of pre-stretching on the samples, the Image-Pro Plus software was applied to count the average size and density of IGPs, showed in Fig. 5. It is found that the average size of IGPs rises from about 2.2 to 3.5, 5.3, 5.8 nm, respectively, while the density declines from about 5.4 × 10^{16} cm^{-3} to 4.6 × 10^{16} cm^{-3}, 3.8 × 10^{16} cm^{-3}, 3.5 × 10^{16} cm^{-3} when the pre-stretching increases gradually. Compared with the unpre-stretched sample, the IGPs of 6% pre-stretched sample show larger size and lower density.

Evolutions of grain boundary precipitates after creep aging

Figure 6 demonstrates the grain boundary precipitates (GBPs) after creep aging at 140 °C for 20 h. It can
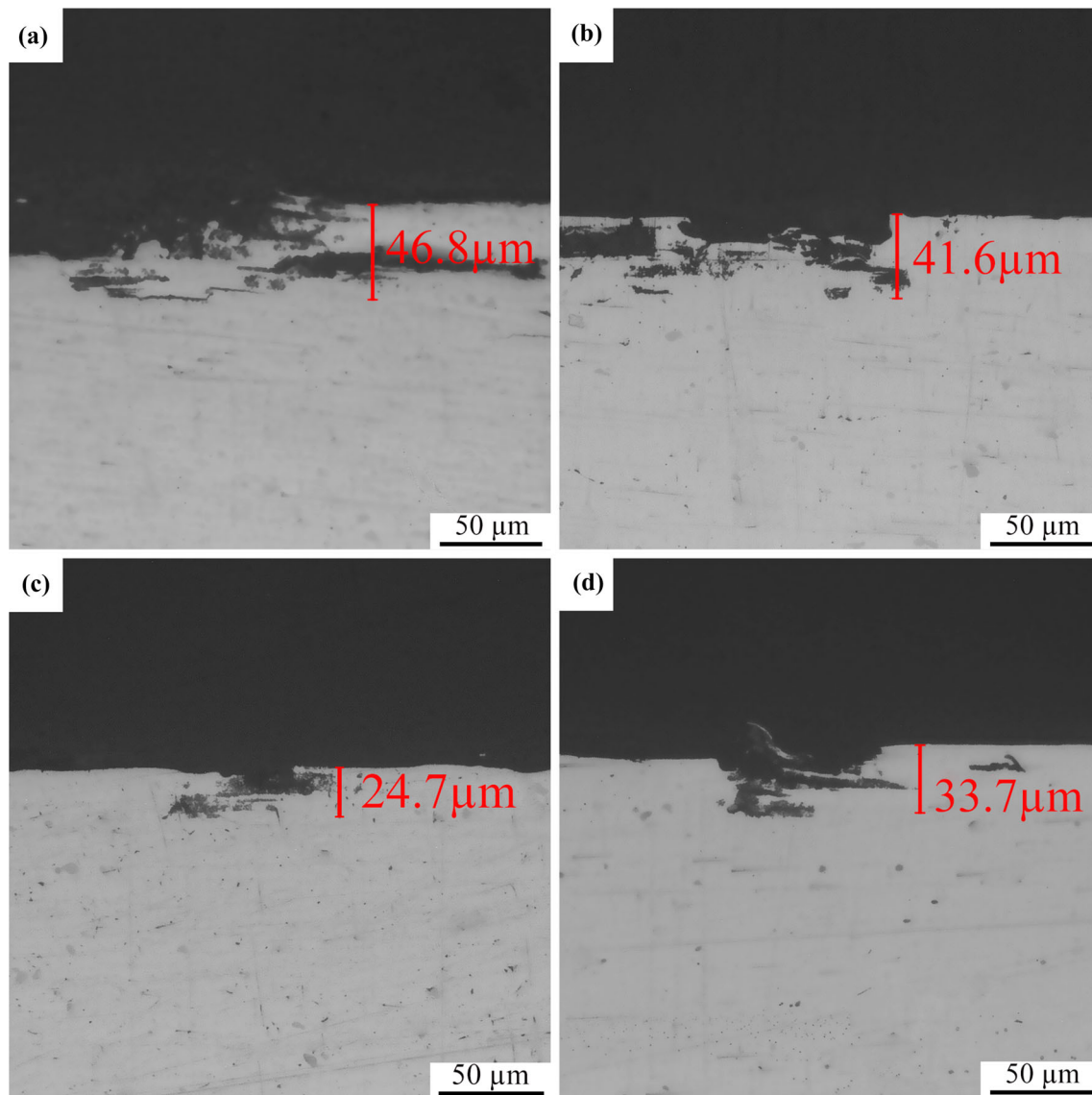
Figure 3 Intergranular corrosion section morphologies of samples with various pre-stretchings after creep aging: **a** 0%; **b** 2%; **c** 4%; **d** 6%.

be seen from Fig. 6a that the precipitates are relatively small, distributing along the grain boundary and there is a narrow precipitation-free zone (PFZ) whose width is about 22.8 nm. Compared with the unpre-stretched sample, the GBPs of 2% pre-stretched specimen are coarser and more discontinuous, and the obvious PFZ is found along the grain boundary, with a width of near 36.7 nm (Fig. 6b). As the pre-stretching increases to 4% and 6%, the GBPs separate from each other and the PFZ width increase to some degree, namely 38.5 and 47.9 nm, respectively (Fig. 6c, d).

For the purpose of identifying the evolution of GBPs, more than ten TEM graphs are counted by Image-Pro Plus software. Figure 7 shows the evolution of the average size and distance of GBPs. It can be observed that the average size of GBPs rises from about 9.3 to 15.7, 21.0, 23.9 nm, respectively, and the average distance between GBPs increases from about 11.8 to 20.4, 32.1, 39.4 nm when the pre-stretching increases gradually. The 4% and 6% pre-stretched samples have coarser and more discontinuous GBPs.

In order to further study the effect of pre-stretchings on the GBPs of the alloy, STEM-EDS line scanning analysis of the main alloy elements Al, Zn, Mg
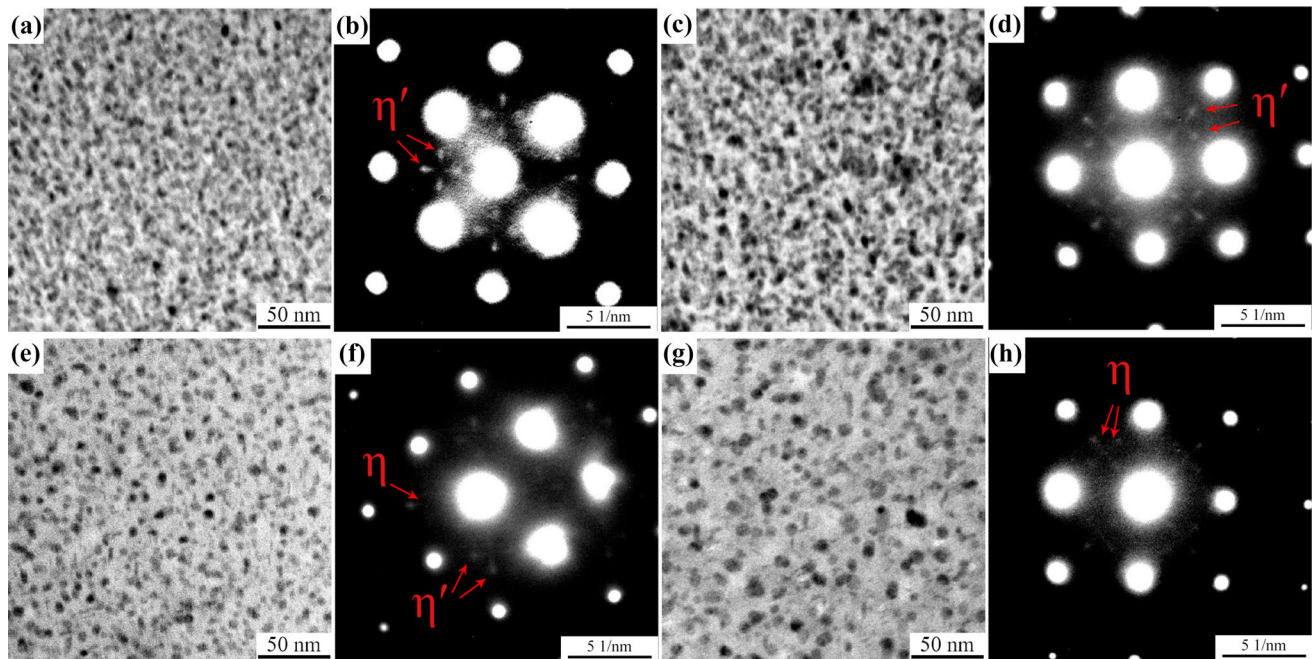
Figure 4 TEM bright field images of IGPs and corresponding SAED patterns of samples with different pre-stretchings: **a** and **b** 0%; **c** and **d** 2%; **e** and **f** 4%; **g** and **h** 6%.
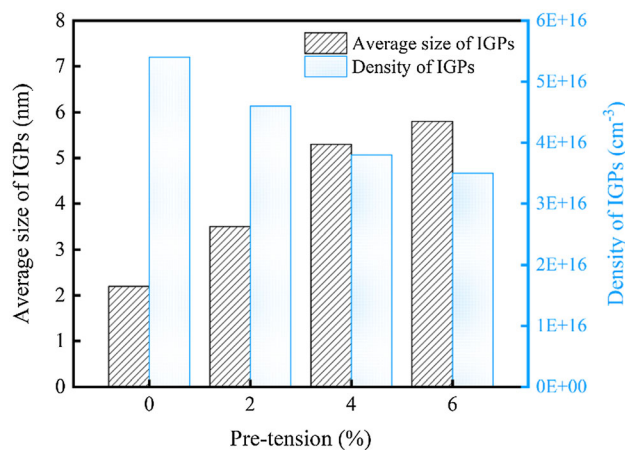

Figure 5 Histogram of average size and density of IGPs with different pre-stretchings.

and Cu is carried out, and the results are showed in Fig. 8. The total composition fluctuations across the grain boundary including coarse precipitates are displayed. The variation of GBP elements in the samples is similar that the degree of segregation of Zn and Mg elements is large, forming obvious convex peaks and the content of Al elements decreases compared with that in the matrix, forming a hollow valley. The degree of Mg segregation at grain boundaries decreases gradually with the increasing pre-stretching. The most apparent segregation of Mg

occurs in the 0% pre-stretched alloy and the 4% pre-stretched alloy has the smoothest curve of Mg. Besides, though the changing trend of Cu content in Fig. 8b, d is not obvious, the level of Cu rises in Fig. 8f, h. The results suggest that the 4% pre-stretched alloy has less Mg segregation and relatively more Cu element.

Dislocation density during creep aging

Dislocations play a key role in creep mechanism in CA process and the dislocation density alters dynamically [9]. In order to figure out the effect of dislocations on precipitates, it is essential to investigate the change of dislocation density. The peak shape broadening of XRD is mostly influenced by lattice strain and grain size [17]. Since the grain size is basically same during the process of CA, the lattice strain is the only factor that has an impact on the expansion of the peak shape. Equation (2) reflects the alteration of lattice strain [9]

$$L_{FWHM}cos(\theta) = \frac{0.9\lambda}{d} + 2\varepsilon sin(\theta) \qquad (2)$$

where L_{FWHM} is the full width at half the maximum of the diffraction peak, θ is half of the diffraction angle, λ is the wavelength, d is the average grain size and ε is the lattice strain. Since the value of ε reflects
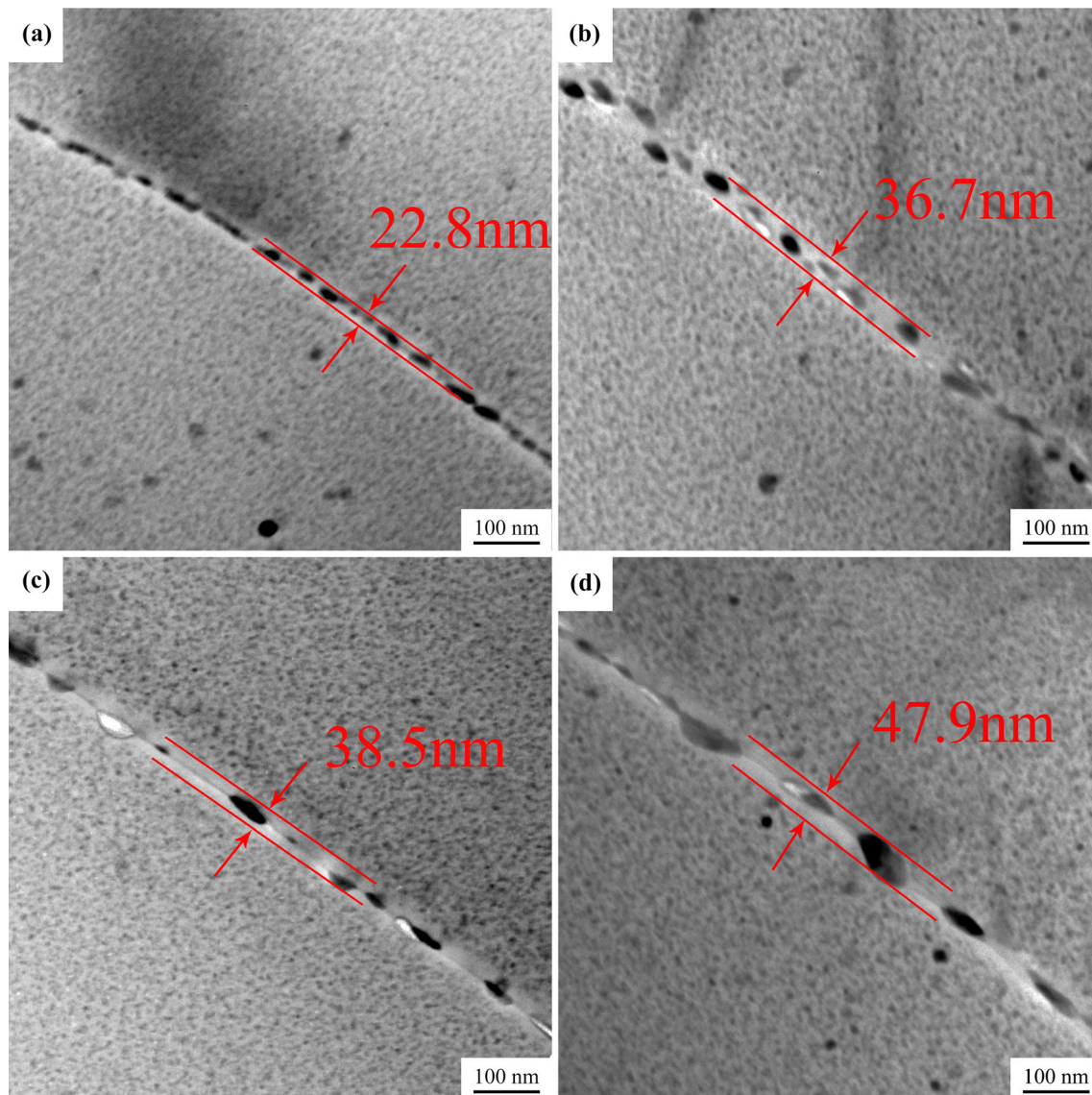
Figure 6 GBPs evolution of the samples under different pre-stretchings: **a** 0; **b** 2%; **c** 4%; **d** 6%..

the dislocation density [18], the evolution of dislocation density can also be reflected by the slope of the L_{FWHM} $cos\theta$-$2sin\theta$. Figure 10 shows the dislocation evolution of the sample with 6% pre-stretching at different stage (0 h, 0.5 h, 10 h represents the pre-stretched stage, the primary stage, the stable stage, respectively) during CA and the corresponding fitting curves of dislocation density. As shown in Fig. 9a, long and curved dislocations appear in the matrix. With the progressing of CA, the dislocations tangle and multiply and it is obvious that there are precipitates prior to nucleate and grow at the tip of

dislocations, exhibiting a larger diameter (Fig. 9b). In the stable stage, the dislocations reduce and the dispersed precipitates distribute evenly (Fig. 9c). As depicted in Fig. 9d, the slope of L_{FWHM} $cos\theta$-$2sin\theta$ fitted line is dropping with the extension of testing time. The ε value of the 6% pre-deformed samples at 0 h, 0.5 h, 10 h is 0.20027, 0.17594, 0.13428, respectively. The dislocation density rises with the participation of pre-stretching, which is beneficial for the nucleation and growth of precipitates, and further affect the size and distribution of precipitates after CA.
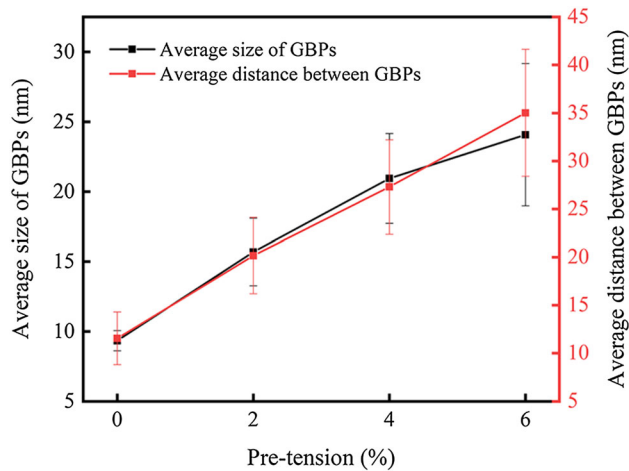
Figure 7 Curves of average size and distance of GBPs under different pre-stretchings.

Discussion

Effects of pre-stretching on microstructure after creep aging

The CA process under stress at high temperature is controlled by various deformation mechanisms, such as thermal diffusion, dislocation motion and grain boundary slip. According to Lei et al. [6], dislocation slip and climbing are the main mechanisms in the CA process of Al–Zn–Mg-Cu alloy. Furthermore, the interaction between dislocations and precipitates has great influence on the size and distribution of precipitates after CA. Precipitation strengthening is the primary strengthening mechanism of 7xxx aluminum alloy [19]. Generally, the precipitation sequence of 7xxx aluminum alloys has been established as: supersaturated solid solution—GP zone- η'—η [20, 21]. GP zone is the region of atomic segregation which is coherent with the matrix, η' is a kind of metastable phase which is semi-coherent and η is an equilibrium phase which is incoherent with the matrix.

During the primary stage of CA, the dislocations promoted by the pre-stretching increases the potential energy of the matrix and provides part of the nucleation energy, thus the pre-stretching is favorable for precipitating during the CA [22]. As Fig. 9a shows, after the introduction of pre-stretching, a large number of dislocations appear in the alloy. With the increase of dislocation density, the elastic interaction among the dislocations, solute atoms and vacancies increases, leading to the diffusion of solute atoms and vacancies around the dislocations into the dislocations [23]. Therefore, the precipitates are easy to nucleate at the dislocation distortion region (Fig. 9b), that is the dislocation provides heterogeneous nucleation area for the precipitates.

At the stable stage of CA, the accumulation and annihilation of dislocations in the material reach a dynamic balance, leading to a stable creep rate [24].
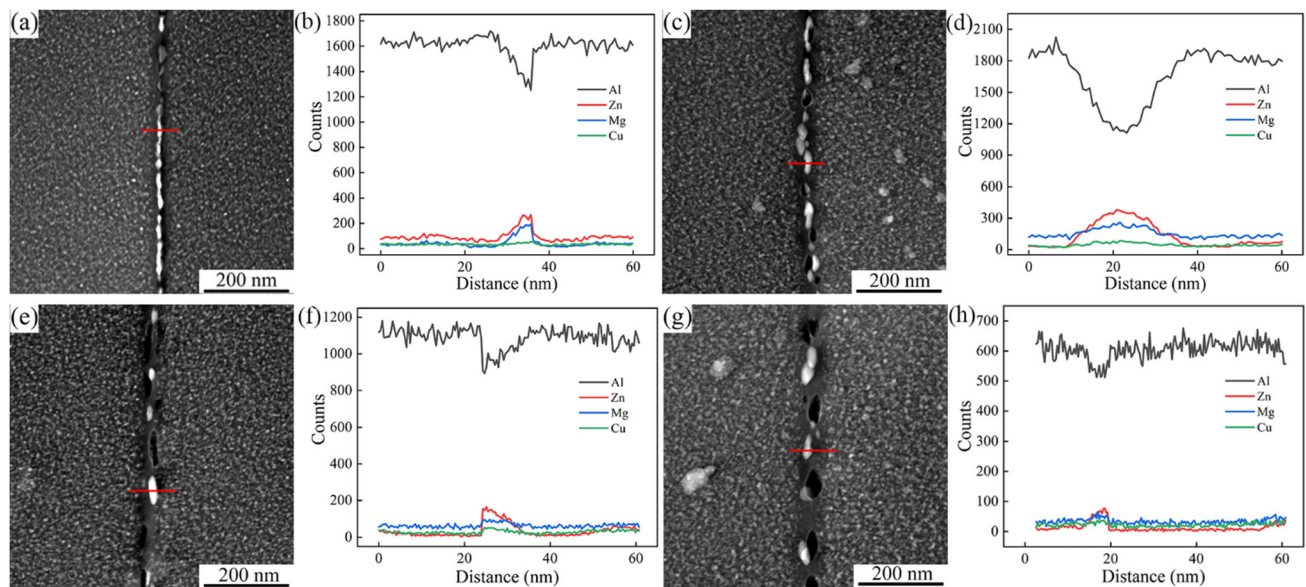

Figure 8 GBPs of samples with various pre-stretchings after CA and corresponding image of detected position by line scanning (the position is indicated by red line): **a** and **b** 0; **c** and **d** 2%; **e** and **f** 4%; **g** and **h** 6%.
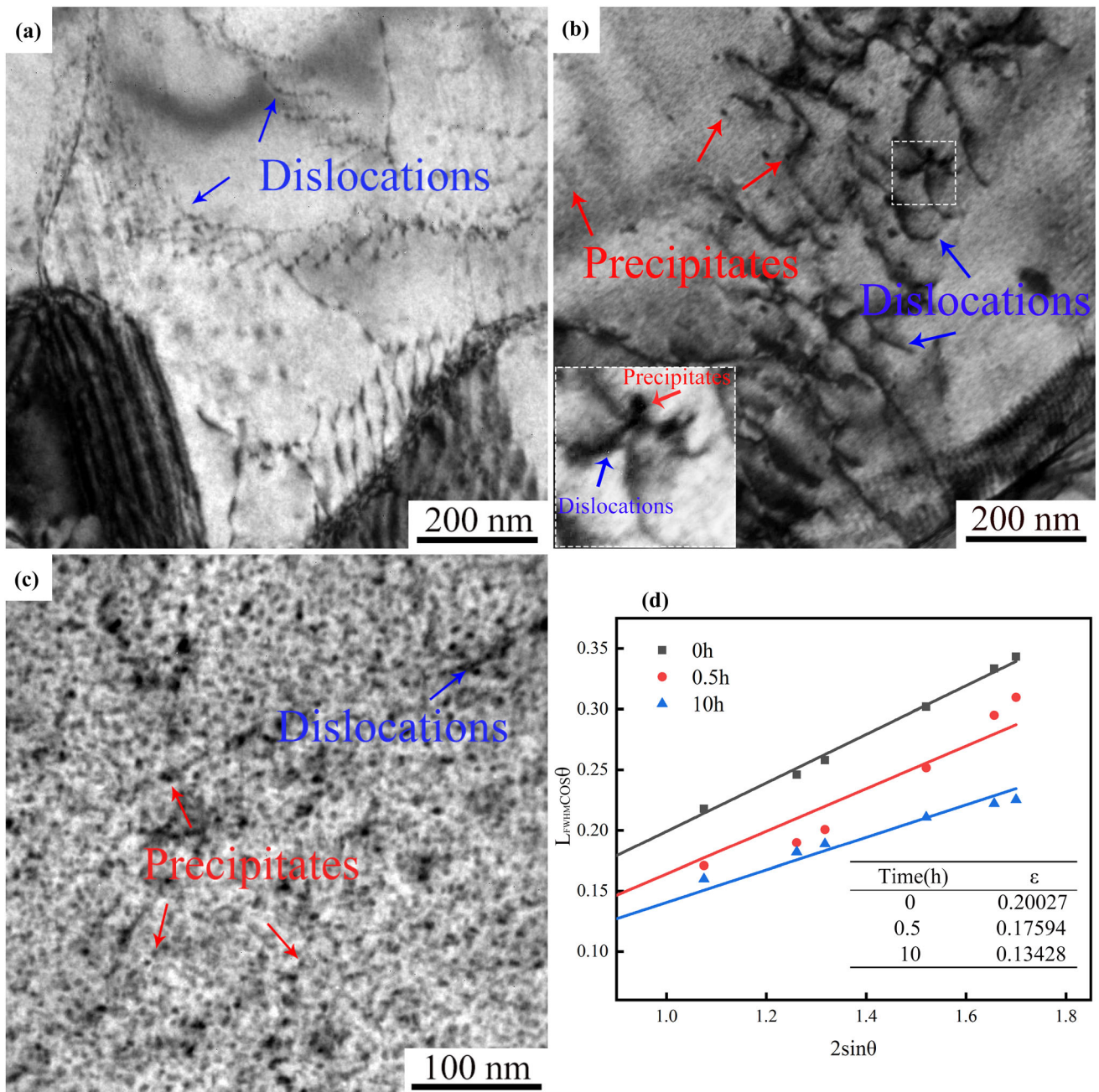
Figure 9 Dislocation evolution of 6% pre-stretched sample at different stage: **a** 0 h; **b** 0.5 h; **c** 10 h; **d** the fitting curves of dislocation density under different stage.

With the progressing of CA, the number of precipitates increases (Fig. 9c). In the samples with larger pre-stretching, more precipitates nucleate and grow adjacent to the numerous dislocations during the aging and then transform from metastable phase η′ to the equilibrium phase η ahead of time in the samples with pre-stretching. At the moment, the solute atoms surrounding the fine precipitates will move to the large precipitates, causing the dissolution of fine precipitates and the growth of large precipitates. The growth process of the precipitations is called Ostwald coarsening. This coarsening mechanism is defined as follows [25]:

$$(\bar{r})^3 - r_0^3 = (D\gamma X_e)t \tag{3}$$

where $\bar{r}$ is the average radius of the precipitates, r_0 is the average radius of the precipitates at t = 0, D, γ, X_e is the diffusion coefficient, the interface energy, the average solid solubility of the large precipitates, respectively. In order to reduce the total interfacial energy, the high-density fine precipitations with high interfacial energy tend to transform to coarse precipitations with low overall interfacial energy [26]. Therefore, the phenomenon of precipitate coarsening occurs and the density of the precipitates decreases. It can be seen from Fig. 5 that the IGPs of the samples with different pre-stretching are different. Compared with the unpre-stretched samples with small size and high density IGPs, the samples with the pre-stretching of 4% and 6% have coarser IGPs and longer intervals between IGPs.

Since the energy is high near the grain boundary, the heterogeneous nucleations of precipitations are more likely to occur and the precipitates are easy to grow up, leading to larger precipitates on the grain boundary than in the matrix. In addition, the GBPs absorb the nearby solute atoms, which results in the solute atoms of surrounding matrix being unable to precipitate, thus forming the PFZ [27]. In this work, the PFZ is narrow and the GBPs are small and continuous in the sample without pre-stretching, as showed in Fig. 6a. While the pre-stretching is carried out before CA, the GBPs grow and the grain boundaries broaden, even PFZ appears (Fig. 7b–d). The 4% and 6% pre-stretched specimen owns the wide PFZ of 38.5, 47.9 nm, respectively, and the discontinuous GBPs. Moreover, with the purpose of figuring out the change of GBPs in more detail, stem-EDS line scanning analysis of the main alloy elements Al, Zn, Mg and Cu is carried out. It can be seen from Fig. 8 that the segregation of Mg is slight and the Cu content of the GBPs is relatively high in 4% pre-deformed sample.

The influence mechanisms of pre-stretching on the microstructure of 0% and 6% pre-stretched sample are shown in Fig. 10. Before conducting the CA, the sample without pre-stretching is a supersaturated solid solution (Fig. 10a1). After applying temperature and stress, the dislocation multiplication occurs in the sample (Fig. 10a2), contributing to the increasing dislocation density. The clusters are rich in solute atoms and some precipitates form on the dislocation lines, causing the lower concentration of solute atoms and uneven distribution of precipitates. As shown in Fig. 10a3, in the stable stage of CA, dislocation

proliferation and annihilation reach a balance and the precipitates are distributed densely, which are mainly metastable phase η′. The precipitates near the grain boundary are larger than the IGPs and the PFZ is narrow. When 6% pre-stretching was applied to the sample, a great deal of dislocations appear in the matrix (Fig. 10b1). It can be seen from Fig. 10b2 that the number of dislocations multiplied in the primary stage and the dislocations are more than that of the sample without pre-stretching. The precipitates are prior to nucleate and grow on the dislocations, and the more dislocations, the faster nucleation. In the stable stage of the 6% pre-stretched sample, since the precipitation is faster, the precipitates transform from η′ to η in advance, and thus small IGPs dissolve to promote the formation of larger IGPs. The coarsening phenomenon occurs and the density of the precipitates decreases (Fig. 10b3). Compared with the sample without pre-stretching, there are coarser GBPs, larger distance between GBPs and wider PFZs in the 6% pre-stretched sample.

Effects of pre-stretching on corrosion resistance after creep aging

The difference of corrosion resistances of various pre-stretched alloys can be explained by the change of matrix precipitations, GBPs and precipitation-free zone (PFZ). It is generally believed that stress corrosion cracking (SCC) is related to the conductivity and affected by the size and distribution of the precipitates [28]. The local distortion caused by the solute atoms has a scattering effect on the electrons, and thus more solute atoms cause stronger scattering effect, resulting in the declining conductivity and weak SCC resistance. As demonstrated in Fig. 5, with the degree of the pre-stretching increasing from 0 to 6%, the precipitates increase in diameter, decrease in density and solute atoms are consumed, so the scattering effect on electrons decreases. Moreover, the coherent GP zone and semi-coherent phase η 'grow into incoherent phase η, leading to the release of strain field around the precipitates, causing better SCC resistance.

At present, the stress corrosion mechanism of 7xxx aluminum alloy is mainly the anodic dissolution [13], hydrogen embrittlement [15] and their combination. The corrosion mode jointly affected by the two mechanisms is that defects are formed by local anodic
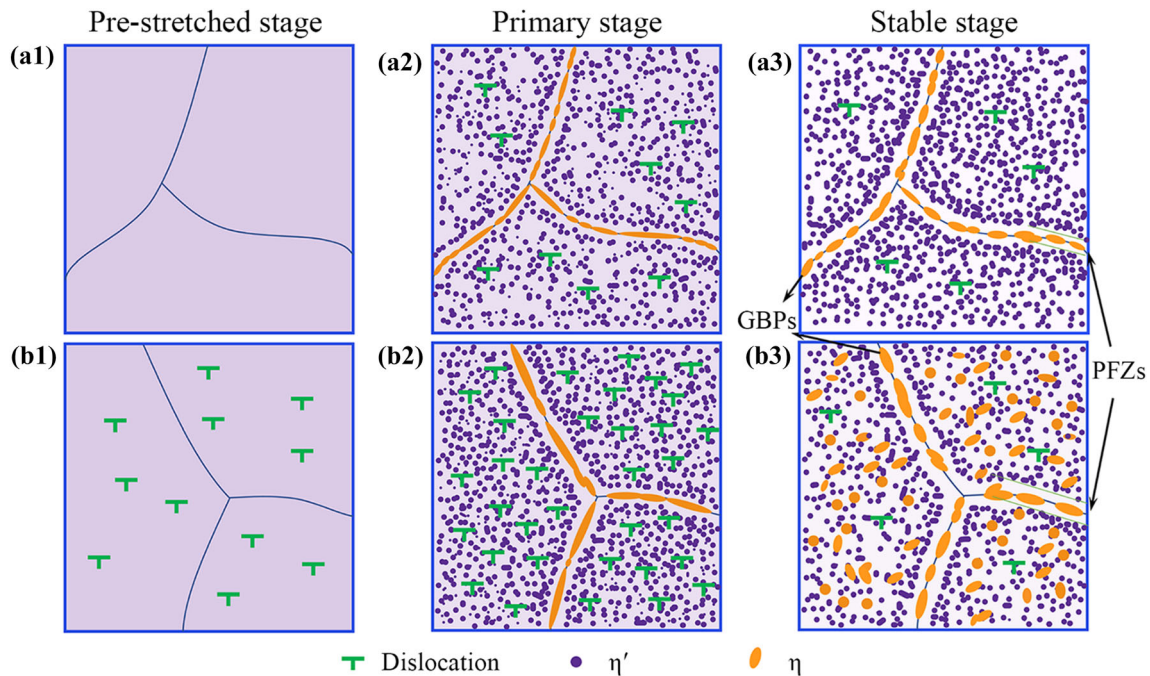
Figure 10 Schematic illustration of the microstructure evolutions of the samples after CA: **a** sample without pre-stretching; **b** sample with 6% pre-stretching.

dissolution firstly, and then hydrogen will gather at the grain boundary and combine to form hydrogen escaping or accumulate to a critical value with the increase of external stress. The binding force between boundaries weakens, resulting in hydrogen-induced cracking (HIC) [29]. Therefore, anode dissolution and HIC coexist during the SCC process. The migration of hydrogen could occur in SSRT, leading to HIC. Since the larger GBPs can capture more migrating H atoms in the initial stage of HIC, more hydrogen can generate and escape from the grain boundary region [30]. It can be observed directly from Fig. 7 that the samples with the pre-stretching of 4% and 6% have larger GBPs, which can delay the brittle fracture of grain boundary to avoid the intergranular SCC. Moreover, due to the variation of the size of precipitates, the main dislocation strengthening mechanism in the alloy changes from cutting to bypassing, which reduces the planar slip of dislocations and leads to a single slip mode [31]. Thus, the aggregation of H atoms through the dislocation to the grain boundary reduces significantly. In general, low concentration of hydrogen atoms in the grain boundary can inhibit the occurrence of hydrogen embrittlement fracture. Therefore, with the transformation and growth of precipitates in the matrix and grain boundaries under

the action of pre-stretchings, the HIC effect is weakened, contributing to a better corrosive resistance.

For anodic dissolution, the precipitations near the grain boundary are η with a potential about -0.86 V, which is the anode phase compared with the aluminum matrix with the potential of -0.68 V [32]. The η phase on the grain boundary dissolves firstly in the corrosive environment, causing the corrosion behavior to proceed along the grain boundary, which is the reason for promoting the extension of intergranular fracture. As presented in Fig. 6a, the sample without pre-stretching has a relatively continuous grain boundary and the corrosion can spread rapidly along the grain boundary, causing poor corrosion resistance, while the 2% pre-stretched specimen has better corrosion performance since the GBPs are more discontinuous (Fig. 6b). When the pre-stretching reaches 4%, as showed in Fig. 6c, the grain boundary becomes discontinuous more apparently, so the rapid expansion channel of corrosion is cut off, leading to better corrosion resistance. As for the 6% pre-stretched specimen, the precipitates around the grain boundary are gradually absorbed and the distance between GBPs expands (Fig. 6d), inducing the discontinuity of the grain boundary more apparently. However, the corrosion resistance of the 6% pre-deformed specimen is lower than the 4% pre-deformed

specimen, which is attributed to the PFZ width. According to Lin et al. [13], the relatively narrow PFZ is conducive to the improvement of corrosion resistance. Since the potential of PFZ differs from the matrix, the anodic dissolution of the GBPs occurs. The expanding of PFZ increases the potential difference between matrix and PFZ, and then promotes the anodic dissolution [33]. The 6% pre-deformed specimen owns the widest PFZ of 47.9 nm, which lead to the lower corrosion resistance than the specimen with 4% pre-stretching.

The element composition of precipitations is also related to the corrosion performance. The segregation of Mg enhances hydrogen absorption at grain boundaries and promotes Mg-H interaction, leading to HIC [34]. As suggested in Fig. 8, the degree of Mg segregation at grain boundaries decreases with the increasing pre-stretching, which can inhibit the formation of Mg-H and thus reduce the susceptibility of SCC. In addition, higher Cu content can reduce the potential difference and delay the occurrence of SCC [35]. Though the changing trend of Cu content is not obvious in Fig. 8b, d, the level of Cu rises when the line scanning gets through the precipitation (Fig. 8f), which contributes to the best corrosion behavior of the 4% pre-deformed sample to a certain extent.

Conclusion

1. Compared with the 0%, 2%, 6% pre-stretched samples, the corrosion performance reaches the optimal value at 4% pre-stretched sample, which owns the largest stress corrosion sensitivity factor r_{tf} (93.8%) and the shallowest intergranular depth (24.7 μm).
2. When the degree of pre-stretching before creep aging rises, coarser and sparser intragranular precipitates (IGPs) are obtained after CA. The average size of IGPs rises from about 2.2 to 5.8 nm while the density declines from about 5.4×10^{16} to 3.5×10^{16} cm^{-3}.
3. When the pre-stretching increases, the grain boundary precipitates (GBPs) become larger and more discontinuous and precipitate-free zones broaden. The average size of GBPs rises from about 9.3 to 23.9 nm, the average distance between GBPs increases from about 11.8 to 39.4 nm and the width of PFZ increases from 22.8 to 47.9 nm. Additionally, the segregation

degree of Mg reduces and the content of Cu of GBPs rises.
4. The coarser and sparser IGPs reduces the scattering effect and releases the strain field. Meanwhile, the coarser and discontinuous GBPs reduce the possibility of anodic dissolution and hydrogen-induced cracking. However, the expanding PFZ increases the potential difference between matrix and PFZ, promoting the anodic dissolution. These factors contribute to the best corrosion resistance in the 4% pre-stretched sample.

Data availability statement

Research data are not shared.

Declarations

Conflict of interest The authors declare no conflict of interest.

References

[1] Peng X, Yao L, Liang X, Qi G, Yin Z (2017) Precipitate behavior and mechanical properties of enhanced solution treated Al–Zn–Mg–Cu alloy during non-isothermal ageing. J Alloy Compd 735:964–974

[2] Lin YC, Zhang JL, Guan L, Liang YJ (2015) Effects of pre-treatments on aging precipitates and corrosion resistance of a creep-aged Al–Zn–Mg–Cu alloy. Mater Des 83:866–875

[3] Yang D, Miao J, Zhang F, Fu Z, Liu Y (2019) Effects of prebending radii on microstructure and fatigue performance of Al–Zn–Mg–Cu aluminum alloy after creep age forming. Metals Open Access Metall J 9(6):630

[4] Lin, Y., C., Peng, Xiao-Bin, Jiang, Yu-Qiang, Shuai, Ci-Jun (2018) Effects of creep-aging parameters on aging

precipitates of a two-stage creep-aged AleZneMgeCu alloy under the extra compressive stress. J Alloys Comp Interdiscip J Mater Sci Solid State Chem Phys, pp 448–455

[5] Zhan L, Lin J, Dean TA (2011) A review of the development of creep age forming: Experimentation, modelling and applications. Int J Mach Tools Manuf 51(1):1–17

[6] Lei C, Yang H, Li H, Shi N, Fu J, Zhan L (2016) Dependence of creep age formability on initial temper of an Al–Zn–Mg–Cu alloy. Chin J Aeronaut 29(005):1445–1454

[7] Jeshvaghani RA, Emami M, Shahverdi HR, Hadavi S (2011) Effects of time and temperature on the creep forming of 7075 aluminum alloy: springback and mechanical properties. Mater Sci Eng, A 528(29–30):8795–8799

[8] Jeshvaghani RA, Zohdi H, Shahverdi HR, Bozorg M, Hadavi S (2012) Influence of multi-step heat treatments in creep age forming of 7075 aluminum alloy: optimization for springback, strength and exfoliation corrosion. Mater Cha 73(none):8–15

[9] Li H, Bian TJ, Lei C, Zheng GW, Wang YF (2018) Dynamic interplay between dislocations and precipitates in creep aging of an Al–Zn–Mg–Cu alloy. Adv Manuf, pp 15–29

[10] Deschamps A, Fribourg G, Bréchet Y, Chemin JL, Hutchinson CR (2012) In situ evaluation of dynamic precipitation during plastic straining of an Al–Zn–Mg–Cu alloy. Acta Mater 60(5):1905–1916

[11] Fribourg G, Bréchet Y, Chemin JL, Deschamps A (2011) Evolution of Precipitate microstructure during creep of an AA7449 T7651 aluminum alloy. Metall Mater Trans A 42(13):3934–3940

[12] Xiao YP, Pan QL, Li WB, Liu XY, He YB (2011) Influence of retrogression and re-aging treatment on corrosion behaviour of an Al–Zn–Mg–Cu alloy. Mater Des 32(4):2149–2156

[13] Lin YC, Jiang YQ, Zhang XC, Deng J, Chen XM (2014) Effect of creep-aging processing on corrosion resistance of an Al–Zn–Mg–Cu alloy. Mater Des 61:228–238

[14] Chen J, Zhang X, Zou L, Yu Y, Li Q (2016) Effect of precipitate state on the stress corrosion behavior of 7050 aluminum alloy. Mater Char, pp 1–8

[15] Jing-Chie, Lin, and, Hsueh-Lung, Liao, and, Wern-Dare, Jehng, and, Chih-Horng (2006) Effect of heat treatments on the tensile strength and SCC-resistance of AA7050 in an alkaline saline solution. Corrosion Sci, pp 3139–3156

[16] Ou BL, Yang JG, Yang CK (2000) Effects of step-quench and aging on mechanical properties and resistance to stress corrosion cracking of 7050 aluminum alloy. Mater Trans JIM 41(7):783–789

[17] Ungár T (2004) Microstructural parameters from X-ray diffraction peak broadening. Scripta Mater 51(8):777–781

[18] Rodgers BI, Prangnell PB (2016) Quantification of the influence of increased pre-stretching on microstructure-strength relationships in the Al–Cu–Li Alloy AA2195. Acta Mater 108:55–67

[19] Bai Z, Qiu F, He Y, Zhao H, Jiang Q (2015) Tensile properties and work-hardening behaviours of Al–Cu alloys modified by Al84Ni10La6metallic glass. Int J Cast Metals Res, pp 352–355

[20] Gang S, Cerezo A (2004) Early-stage precipitation in Al–Zn–Mg–Cu alloy (7050). Acta Mater 52(15):4503–4516

[21] Buha J, Lumley RN, Crosky AG (2008) Secondary ageing in an aluminium alloy 7050. Mater Sci Eng A 492(1–2):1–10

[22] Deschamps A, Livet F, Bréchet Y (1998) Influence of pre-deformation on ageing in an Al–Zn–Mg alloy—I. Microstructure evolution and mechanical properties. Acta Mater 47(1):281–292

[23] Lin YC, Jiang YQ, Chen XM, Wen DX, Zhou HM (2013) Effect of creep-aging on precipitates of 7075 aluminum alloy. Materials Science & Engineering A 588 (dec.20):347–356

[24] Blum W, Eisenlohr P, Breutinger F (2002) Understanding creep—a review. Metall Mater Trans A 33(2):291–303

[25] Wen YH, Wang Y, Chen LQ (2002) Coarsening dynamics of self-accommodating coherent patterns. Acta Mater 50(1):13–21

[26] Tsumuraya K, Miyata Y (1983) Coarsening models incorporating both diffusion geometry and volume fraction of particles. Acta Metall 31(3):437–452

[27] Peng X, Li Y, Xu G, Huang J, Yin Z (2018) Effect of precipitate state on mechanical properties, corrosion behavior, and microstructures of Al–Zn–Mg–Cu alloy. Met Mater Int 24(5):1046–1057

[28] Peng X, Qi G, Liang X, Ying D, Yi G, Xu G, Yin Z (2017) Mechanical properties, corrosion behavior and microstructures of a non-isothermal ageing treated Al–Zn–Mg–Cu alloy. Mater Sci Eng A 688:146–154

[29] Song RG, Dietzel W, Zhang BJ, Liu WJ, Tseng MK, Atrens A (2004) Stress corrosion cracking and hydrogen embrittlement of an Al–Zn–Mg–Cu alloy. Acta Mater 52(16):4727–4743

[30] Christodoulou L, Flower HM (1980) Hydrogen embrittlement and trapping in Al6%–Zn–3%Mg. Acta Metall 28(4):481–487

[31] Chuang TCTTH (1997) Role of grain size on the stress corrosion cracking of 7475 aluminum alloys. Mater Sci Eng A 225(1–2):135–144

[32] Lei C, Yang H, Li H, Shi N, Zhan LH (2017) Dependences of microstructures and properties on initial tempers of creep aged 7050 aluminum alloy. J Mater Process Technol 239:125–132

[33] Jiang F, Huang J, Jiang Y, Xu C (2021) Effects of quenching rate and over-aging on microstructures, mechanical properties and corrosion resistance of an Al–Zn–Mg (7046A) alloy. J Alloys Comp 854:157272

[34] Song RG, Tseng MK, Zhang BJ, Liu J, Jin ZH, Shin KS (1996) Grain boundary segregation and hydrogen-induced fracture in 7050 aluminium alloy. Acta Mater 44(8):3241–3248

[35] Marlaud T, Deschamps A, Bley F, Lefebvre W, Baroux B (2010) Influence of alloy composition and heat treatment on precipitate composition in Al–Zn–Mg–Cu alloys. Acta Mater 58(1):248–260